

12-20-2022

## Magnetized inulin by Fe<sub>3</sub>O<sub>4</sub> as a bio-nano adsorbent for treating water contaminated with methyl orange and crystal violet dyes

Kamran Valizadeh

Amir Bateni

Nazanin Sojoodi

Maryam Rostami Ataabadi

Amir Hossein Behroozi

*See next page for additional authors*

Follow this and additional works at: <https://ro.ecu.edu.au/ecuworks2022-2026>



Part of the [Chemical Engineering Commons](#)

---

[10.1038/s41598-022-26652-7](https://doi.org/10.1038/s41598-022-26652-7)

Valizadeh, K., Bateni, A., Sojoodi, N., Ataabadi, M. R., Behroozi, A. H., Maleki, A., & You, Z. (2022). Magnetized inulin by Fe<sub>3</sub>O<sub>4</sub> as a bio-nano adsorbent for treating water contaminated with methyl orange and crystal violet dyes. *Scientific Reports*, 12, Article 22034.

<https://doi.org/10.1038/s41598-022-26652-7>

This Journal Article is posted at Research Online.

<https://ro.ecu.edu.au/ecuworks2022-2026/1664>

---

**Authors**

Kamran Valizadeh, Amir Bateni, Nazanin Sojoodi, Maryam Rostami Ataabadi, Amir Hossein Behroozi, Ali Maleki, and Zhenjiang You



OPEN

## Magnetized inulin by $\text{Fe}_3\text{O}_4$ as a bio-nano adsorbent for treating water contaminated with methyl orange and crystal violet dyes

Kamran Valizadeh<sup>1</sup>, Amir Bateni<sup>1</sup>, Nazanin Sojoodi<sup>2</sup>, Maryam Rostami Ataabadi<sup>3</sup>, Amir Hossein Behroozi<sup>3</sup>, Ali Maleki<sup>4</sup>✉ & Zhenjiang You<sup>5,6</sup>✉

Current work focuses on fabricating a new bio-nano adsorbent of  $\text{Fe}_3\text{O}_4$ @inulin nanocomposite via an in-situ co-precipitation procedure to adsorb methyl orange (MO) and crystal violet (CV) dyes from aqueous solutions. Different physical characterization analyses verified the successful fabrication of the magnetic nanocomposite. The adsorbent performance in dye removal was evaluated by varying initial dye concentration, adsorbent dosage, pH and temperature in 5110 mg/L, 0.10.8 g/L, 111 and 283–338 K, respectively. Due to the pH of zero point of charge and intrinsic properties of dyes, the optimum pHs were 5 and 7 for MO and CV adsorption, respectively. The correlation of coefficient ( $R^2$ ) and reduced chi-squared value were the criteria in order to select the best isotherm and kinetics models. The Langmuir model illustrated a better fit for the adsorption data for both dyes, demonstrating the maximum adsorption capacity of 276.26 and 223.57 mg/g at 338 K for MO and CV, respectively. As well, the pseudo-second-order model showed a better fitness for kinetics data compared to the pseudo-first-order and Elovich models. The thermodynamic parameters exhibited that the dye adsorption process is endothermic and spontaneous, which supported the enhanced adsorption rate by increasing temperature. Moreover, the nanocomposite presented outstanding capacity and stability after 6 successive cycles by retaining more than 87% of its initial dye removal efficiency. Overall, the magnetized inulin with  $\text{Fe}_3\text{O}_4$  could be a competent adsorbent for eliminating anionic and cationic dyes from water.

Rapid industrialization and growing human activities have prompted severe environmental concerns worldwide, notably water pollution. Usually, various organic and inorganic contaminants end up in water bodies from different industrial sectors every day<sup>1,2</sup>. Predominantly, textile, plastic, cosmetic and paper production industries continually release toxic dye contaminants into surface waters, negatively impacting the environment, humans and animals<sup>3</sup>. Many commercial dyes are available worldwide, exceeding 10,000 specimens, producing approximately  $7 \times 10^5$  metric tons of dyes per year<sup>4</sup>. The significant contribution of environmental pollution by dyes is related to industrial wastewater by 20%; only about 12% of dyes are wastes from manufacturing and handling processes. The current critical concern is that a significant portion of effluents containing dyes gets discharged to the adjacent water sources without any treatment<sup>5</sup>.

The presence of such dyes in water is not favorable because they decrease the sunlight penetration through water, reducing the photosynthesis mechanism of aquatic plants. Moreover, these dyes are detrimental to living organisms because of various toxic elements, including aromatics, chloride, and heavy metals<sup>6</sup>. Even in a trace

<sup>1</sup>Department of Chemical Engineering, Science and Research Branch, Islamic Azad University, Tehran, Iran. <sup>2</sup>Department of Chemical Engineering, South Tehran Branch, Islamic Azad University, Tehran, Iran. <sup>3</sup>School of Chemical, Petroleum and Gas Engineering, Iran University of Science and Technology, Tehran, Iran. <sup>4</sup>Catalysts and Organic Synthesis Research Laboratory, Department of Chemistry, Iran University of Science and Technology, Tehran 16846-13114, Iran. <sup>5</sup>Center for Sustainable Energy and Resources, Edith Cowan University, Joondalup, WA 6027, Australia. <sup>6</sup>School of Chemical Engineering, The University of Queensland, Brisbane, QLD 4072, Australia. ✉email: maleki@iust.ac.ir; zhenjiang.you@gmail.com

amount, the water-containing dyes could create several health risks in humans, such as cancer, skin problems, and allergic dermatitis<sup>7</sup>. Methyl orange (MO) is a common water-soluble organic synthetic, azo-anionic dye, which is highly carcinogenic, teratogenic, and harmful to organisms and the environment. Also, crystal violet (CV) is a highly toxic and triphenylmethane cationic dye. Its existence in water can cause severe health and environmental problems due to its potent clastogenic nature. Thus, the water contaminated with such dyes should be treated instantaneously worldwide. However, it is not a simple and easy process because of their non-biodegradability, thermal and photostability<sup>8,9</sup>.

Wastewater-containing dyes has been treated by chemical, biological, and physical treatment techniques, including membrane filtration<sup>10</sup>, coagulation<sup>11</sup>, electro dialysis<sup>12</sup>, photocatalytic degradation<sup>13</sup>, adsorption<sup>14</sup>, and chemical oxidation<sup>15</sup>. Among them, adsorption has received much attention due to its superior features. The ease of operation, cost-effectiveness, low operating temperature, no secondary pollution, simplicity, and simultaneous removal of pollutants are great examples of adsorption benefits compared to other methods<sup>16</sup>. Various adsorbents, such as carbonaceous materials, have been used for this purpose thus far. However, their applications in treating dye-polluted water are usually restricted due to their high regeneration cost, low sorption efficiency, and complicated separation process<sup>17</sup>.

In recent three years, several researchers have attempted to develop new chitosan-based bio-nanocomposites magnetized with metal oxides as sustainable adsorbents for water and wastewater treatment<sup>18</sup>. Jawad et al.<sup>19</sup> fabricated a new hybrid bio-adsorbent of crosslinked chitosan-epichlorohydrin/TiO<sub>2</sub> nanocomposite for removing reactive red 120 dye from an aqueous solution, achieving the maximum adsorption capacity of 210 mg/g at 30°C. They found that electrostatic attraction, H-bonding, and  $n-\pi$  stacking are responsible for the adsorption of dye molecules on the adsorbent surface. Reghioua et al.<sup>20</sup> synthesized a Schiff's base chitosan-glutaraldehyde composite magnetized by Fe<sub>3</sub>O<sub>4</sub> and ZnO to remove Remazol brilliant blue R dye from wastewater. The highest capacity was found to be 176.6 mg/g at 60 °C by incorporating 25% ZnO into the nanocomposite structure. Kazemi and Javanbakht<sup>21</sup> fabricated a magnetic zeolite/chitosan/alginate nanocomposite crosslinked by CaCl<sub>2</sub> and glutaraldehyde to enhance its stability. The results indicated a spontaneous exothermic mechanism of methylene blue adsorption by the synthetic adsorbent.

Al-Musawi et al.<sup>22</sup> coated a chitosan polymer with magnetite Fe<sub>2</sub>O<sub>3</sub> nanoparticles to adsorb acid blue 113 dye from an aqueous solution under various experimental factors, such as initial dye concentration, solution pH, nanocomposite dosage, adsorption time and temperature. They found a maximum uptake capacity and dye removal efficiency of 128 mg/g and 99.63% under the optimum conditions, respectively. Tanhaei et al.<sup>23</sup> synthesized a chitosan-based adsorbent magnetized with carbon-Fe<sub>3</sub>O<sub>4</sub> core-shell nanoparticles for methyl orange removal from aqueous solutions with a maximum uptake capacity of 425 mg/g at 45 °C. Neves et al.<sup>24</sup> magnetized chitosan with a novel graphene oxide derivative, grafted long-chain quaternary ammonium salt with arenediazonium salts, to improve its amphiphilic feature and expand the adsorption spectrum. The magnetized sorbent obtained a maximum dye removal capacity and rate of 650 mg/g and 95%, respectively. Their magnetic composite exhibited the potential of being a filtering agent with simple removal from aqueous solutions via the magnet field after each use for removing basic brown 4.

Recently, Hernández-Martínez et al.<sup>25</sup> reported that inulin could be a suitable replacement for chitosan, particularly for removing Pb<sup>2+</sup> from wastewater, to enhance the scalability and production cost of polyurethane based-nanocomposite fabrication. Inulin is a combination of linear fructose polymers with various chain lengths and a glucose molecule at every C2 end, belonging to the fructan group of polysaccharides<sup>26</sup>. As a Generally Recognized as Safe (GRAS) substance, inulin can be produced by a host of microorganisms, which can be extensively detected in nature as a storage carbohydrate. Inulin is commercially made from chicory and partially dissolved in water, enabling it to add to aqueous media without precipitation<sup>27</sup>. Figure S1 (Supplementary) illustrates the general production process of inulin from chicory.

This work aims to fabricate a new biocompatible adsorbent of Fe<sub>3</sub>O<sub>4</sub>@inulin nanocomposite for removing cationic and anionic dyes from water for the first time. The prepared adsorbent was characterized by various analyses, such as scanning electron microscopy (SEM) with energy dispersive X-Ray analysis (EDX), X-ray powder diffraction (XRD), Fourier-transform infrared spectroscopy (FTIR), vibrating sample magnetometry (VSM), Brunauer–Emmett–Teller (BET), and thermogravimetric analysis (TGA). Moreover, kinetics and isotherm studies assessed the adsorption of MO and CV dyes with the synthesized adsorbent. Finally, the adsorbent reusability was checked after several cycles of reusing.

## Materials and methods

**Materials.** Iron (II) chloride tetrahydrate (FeCl<sub>2</sub>·4H<sub>2</sub>O (aq)), Iron (III) chloride hexahydrate (FeCl<sub>3</sub>·6H<sub>2</sub>O (aq)), ammonia (NH<sub>3</sub>, 25%), hydrochloric acid (HCl, 0.1 M), sodium hydroxide (NaOH, 0.1 M), inulin from chicory, methyl orange and crystal violet dyes were purchased from Sigma-Aldrich company. All materials were used in their analytical grades without any further purification. The molecular structures of methyl orange and crystal violet as dye contaminants are depicted in Fig. 1a,b, respectively.

**Synthesis of Fe<sub>3</sub>O<sub>4</sub>@inulin.** First, 60 mL of deionized water was added to a 250 mL two-mouth glass flask. The amount of 0.7 g of FeCl<sub>2</sub>·4H<sub>2</sub>O was poured into the flask under stirring, and then the amount of 1.9 g of FeCl<sub>3</sub>·6H<sub>2</sub>O was added to the solution. The mixture was stirred for 5 min until completely dissolved to obtain a uniform solution. Next, 0.75 g of inulin was slowly added to the solution in several steps under stirring for 25 min. The ambient temperature was raised to 85 °C under a nitrogen atmosphere, and 10 mL of NH<sub>3</sub>OH was injected dropwise by syringe for 70 min. The color of the solution turned black, indicating the formation of Fe<sub>3</sub>O<sub>4</sub> nanoparticles during the injection. The mixture was further stirred for 30 min to allow the remaining NH<sub>3</sub>OH to react. Next, the magnetized inulin nanoparticles were separated from the solution with a magnet and washed

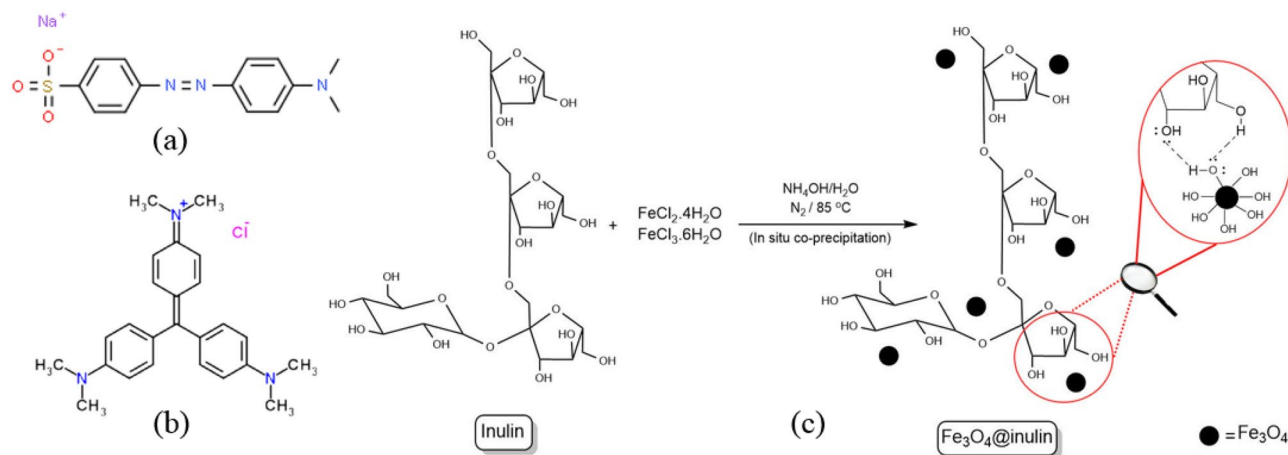


**Figure 1.** Molecular structures of (a) methyl orange, (b) crystal violet, and (c)  $\text{Fe}_3\text{O}_4$ @inulin with synthesis procedure.

with deionized water four times to remove the unreacted materials from the nanocomposite. The magnetized inulin was transferred to an oven and placed at 55 °C for 15 h to dry. Finally, the powdered nanoparticles were obtained for the experiments and characterization. Figure 1c illustrates the molecular scheme of the synthesis procedure of  $\text{Fe}_3\text{O}_4$ @inulin.

**Characterization.** The crystal network of the synthesized adsorbent nanoparticles was examined by an XRD analysis (STOE STADI-MP model, Germany) with Cu K $\alpha$  radiation ( $\lambda = 1.54 \text{ \AA}$ ) and  $2\theta$  of 10°–80°. The adsorbent functional groups were evaluated using the FTIR analysis (Spectrum Rx1 model, Perkin Elmer Co.) in 400–4000  $\text{cm}^{-1}$ . The magnetization property of the prepared nanocomposite was assessed by a VSM device (LBKFB model, Iran) under the ambient condition and in the range of –4000 to 4000 Oe. The structure, morphology and elemental distribution of the adsorbent were identified by SEM–EDX analysis (MIRA3 TESCAN). By heating the sample at 120 °C to eliminate any impurities in its structure, it was analyzed by BET analysis (Micromeritics, Model ASAP 2020, USA) at 77 K. Several  $\text{NaNO}_3$  solutions (0.1 M) with 50 mL volume were added to different flasks at the ambient condition to measure the point of zero charges (PZC). The initial pH values ( $\text{pH}_i$ ) were adjusted by adding HCl and NaOH solutions determined by a pH meter (Crison, Spain). 2 g of sample was added to each solution and then stirred for 48 h under ambient conditions. The final pH values ( $\text{pH}_f$ ) can be measured to calculate the pH of zero point of charge ( $\text{pH}_{\text{ZPC}}$ ).

**Adsorption experiments.** The dye removal experiments have been conducted to determine the adsorption performance of synthesized magnetic nanocomposites as follows. The batch adsorption was carried out in an Erlenmeyer flask with a volume of 250 mL by adding 0.1–0.8 g of the magnetic bio-nano adsorbent in the controlled operational conditions for the isotherm and kinetics investigations. The initial concentration ( $C_{\text{dye}}$ ) of MO and CV varied in the range of 25–200 mg/L. The volume of every solution was 100 mL, and the adsorption temperature was changed from 10 to 65°C. The solution pH was considered in the range of 1–11 to find the best conditions for each dye removal. To do so, the calibration curves were first plotted for both dyes at different pHs. Next, the adsorption experiments were conducted at different pHs and various adsorption times (15–180 min, every 15 min sampling). Finally, the calibration curve with the pH proportional to the corresponding solution pH was used to measure the concentration of the remaining dye in the aqueous solution. The dye concentration was determined by UV–Vis spectrophotometer (Rayleigh/UV 2601) at a wavelength of 464 nm and 590 nm for MO and CV, respectively. The formulas of the removal efficiency and adsorption capacity ( $Q$ ) are as follows<sup>28</sup>:

$$\text{Removal (\%)} = \frac{C_0 - C_e}{C_0} \times 100 \quad (1)$$

$$Q \text{ (mg/g)} = \frac{(C_0 - C_e)V}{m} \quad (2)$$

in which,  $C_0$  and  $C_e$  (mg/L) are the initial and equilibrium concentrations of dyes in the aqueous solution, respectively. The terms  $m$  (g) and  $V$  (L) are the mass of the nanocomposite and the volume of the aqueous solution, respectively. Each experimental run was repeated three times, and all reported results are the averaged data with a deviation error of  $\pm 5\%$ .

## Results and discussion

**Adsorbent characterization.** FTIR analysis is a practical tool for detecting the functional groups in the structure of materials. Figure 2a presents the FTIR spectra of  $\text{Fe}_3\text{O}_4$ , inulin, and  $\text{Fe}_3\text{O}_4$ @inulin compounds. In the  $\text{Fe}_3\text{O}_4$  spectrum, there is a prominent peak related to the FeO bond at 578  $\text{cm}^{-1}$ <sup>29</sup>. The FTIR spectra of inulin

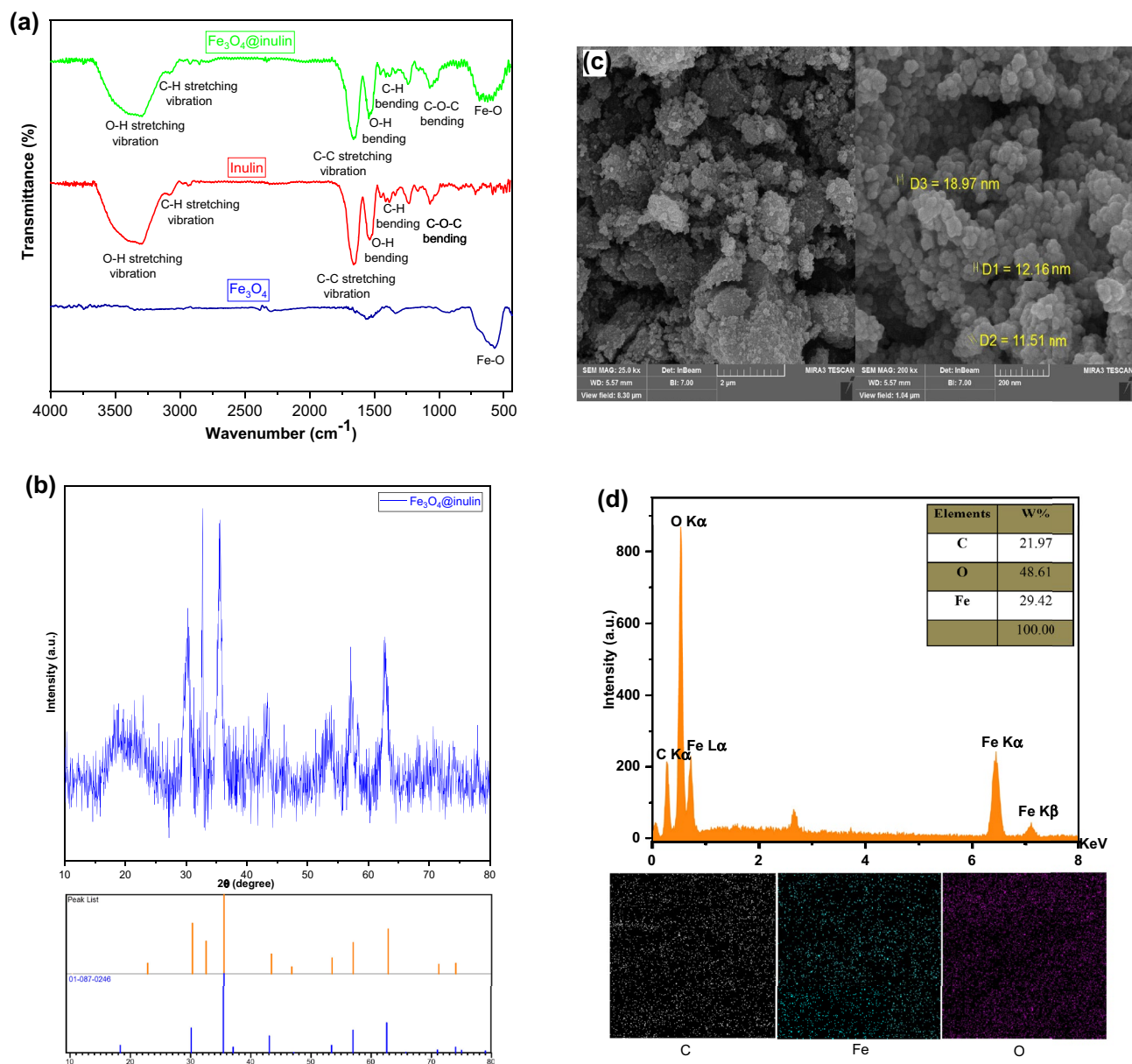


**Figure 2.** (a) FTIR spectra of  $\text{Fe}_3\text{O}_4$ , inulin, and  $\text{Fe}_3\text{O}_4$ @inulin; (b) XRD pattern of the prepared  $\text{Fe}_3\text{O}_4$ @inulin nanocomposite; (c) SEM images and (d) EDX results of the synthesized  $\text{Fe}_3\text{O}_4$ @inulin bio-nano adsorbent.

and  $\text{Fe}_3\text{O}_4$ @inulin nanocomposite illustrate several similar adsorption bands: broad adsorption bands at  $3428$  and  $1531$   $\text{cm}^{-1}$  are attributed to the bending and stretching vibration of the OH bond, respectively<sup>30</sup>, which is abundant in the inulin backbone. The adsorption band at about  $3095$   $\text{cm}^{-1}$  is associated with the stretching vibration of the CH bond<sup>31</sup>. The peak at  $1101$   $\text{cm}^{-1}$  is related to the asymmetric stretching vibration of the COC bond, and an absorption band at  $1052$   $\text{cm}^{-1}$  is attributed to the stretching vibration of the CO bond<sup>32</sup>. Furthermore, the appearance of FeO peak in the  $\text{Fe}_3\text{O}_4$ @inulin spectrum confirms the successful fabrication of the nanocomposite.

The crystalline structure of  $\text{Fe}_3\text{O}_4$ @inulin nanocomposite studied by XRD analysis is shown in Fig. 2b. The individual weak broad peak around  $15^\circ$ – $23^\circ$  indicates the amorphous phase of inulin. According to the standard patterns of  $\text{Fe}_3\text{O}_4$  in card no. JCPDS, 01-087-0246, this magnetic material has some broad characteristic diffraction peaks at  $2\theta$  of  $18.27^\circ$ ,  $30.07^\circ$ ,  $35.46^\circ$ ,  $37.13^\circ$ ,  $43.02^\circ$ ,  $57.16^\circ$ ,  $62.74^\circ$ ,  $71.21^\circ$ , and  $73.49^\circ$ <sup>32</sup>. Sharp and broad peaks demonstrate the crystalline and amorphous areas in the  $\text{Fe}_3\text{O}_4$ @inulin nanocomposite, respectively. Based on Scherer's equation<sup>33</sup>, the average crystalline size for  $\text{Fe}_3\text{O}_4$ @inulin bio-nano adsorbent is  $10.9$  nm.

SEM-EDX analysis of the  $\text{Fe}_3\text{O}_4$ @inulin adsorbent has been conducted to evaluate its morphology and elemental distribution, as presented in Fig. 2c,d. As shown in Fig. 2c at low magnification, the surface morphology of  $\text{Fe}_3\text{O}_4$ @inulin nanocomposite is rough, heterogeneous and irregular with some cavities. However, according to the SEM images at higher magnifications, the adsorbent surface depicts a relatively uniform, regular



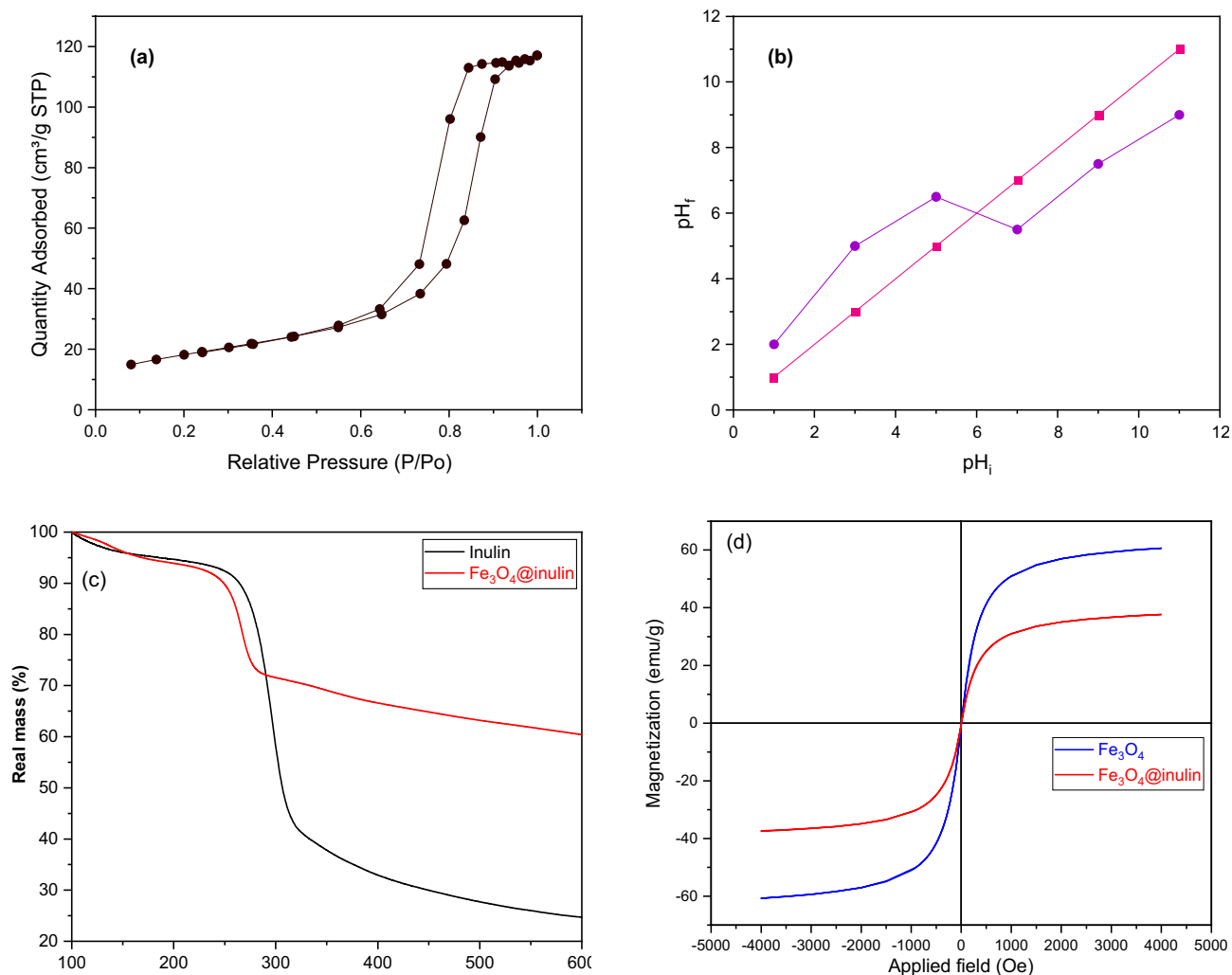


**Figure 3.** (a)  $N_2$  adsorption/desorption curve of the  $Fe_3O_4@inulin$  adsorbent; (b)  $pH_f$  versus  $pH_i$  for determining  $pH_{PZC}$  of the  $Fe_3O_4@inulin$  nanocomposite; (c) TGA curves of inulin and  $Fe_3O_4@inulin$ ; (d) magnetic hysteresis curves of  $Fe_3O_4$  and  $Fe_3O_4@inulin$ .

distribution of spherical nanoparticles on the  $Fe_3O_4@inulin$  nanocomposite surface, with a particle diameter range of 10–20 nm. Moreover, the elemental mapping in Fig. 2d illustrates a uniform distribution of all elements, including carbon, oxygen and iron, within the adsorbent structure, exhibiting the maximum content of oxygen with a contribution of 48.61%.

$N_2$  adsorption/desorption isotherm of the synthesized  $Fe_3O_4@inulin$  nanoparticles is shown in Fig. 3a, resulting from the BET analysis. This curve exhibits the mesoporous structure of the adsorbent supported by the type IV isotherm based on the IUPAC classification<sup>34</sup>. Such mesopores are favorable for enhancing the specific surface area of the material. According to the calculations by the BJH method<sup>35</sup>, the specific surface area of  $66.15\text{ m}^2/\text{g}$ , pore volume of  $0.181\text{ cm}^3/\text{g}$ , and average pore diameter of  $11.027\text{ nm}$  are obtained for  $Fe_3O_4@inulin$  adsorbent. The factor  $pH_{PZC}$  shows the charge of the adsorbent surface, the pH value where the net surface charge is zero. The  $pH_f$  against  $pH_i$  values are plotted in Fig. 3b to determine this factor for the prepared  $Fe_3O_4@inulin$  composite, indicating a  $pH_{PZC}$  of approximately 6. Therefore, the adsorbent surface will be negatively charged at pH values higher than 6, while it will be positively charged otherwise.

The TGA method has been used to assess the thermal resistance of magnetic  $Fe_3O_4@inulin$  in the temperature range of 100–600 °C under an air atmosphere. Figure 3c illustrates the weight loss curve of pure inulin and  $Fe_3O_4@inulin$  materials. Both substances have initially experienced a weight loss of about 9% due to the elimination of free water and moisture evaporation. The most significant decomposition rate related to inulin exists in the range of 240–310 °C with a reduction in its weight by about 50%, which might be associated with dehydration. However, the most considerable weight loss of the  $Fe_3O_4@inulin$  nanocomposite occurs at 240–285 °C with a reduction of approximately 20%, representing the primary degradation of magnetic composite possibly caused by selective dehydration. The residual weights until 600 °C for inulin and  $Fe_3O_4@inulin$  are about 25% and 65%, respectively. As a result, adding magnetic  $Fe_3O_4$  nanoparticles into the inulin matrix can significantly increase its thermal stability due to strong intermolecular interactions. The magnetic characteristic of magnetized inulin is evaluated by VSM analysis. Figure 3d depicts the magnetic hysteresis loop of  $Fe_3O_4$  and  $Fe_3O_4@inulin$ .

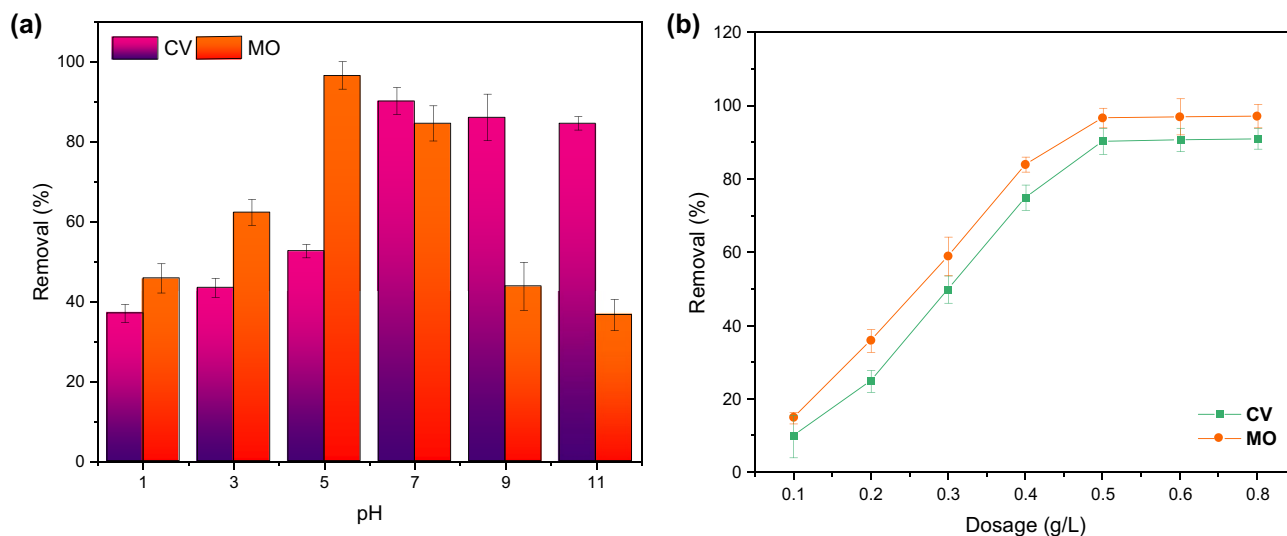


**Figure 4.** (a) Effect of solution pH ( $C_a = 0.5$  g/L,  $C_{dye} = 25$  mg/L); (b) Effect of adsorbent dosage (optimum pH = 7 for CV and 5 for MO) on the dye removal efficiency;  $T = 25$  °C,  $t = 180$  min.

inulin nanoparticles. The magnetic saturation of  $\text{Fe}_3\text{O}_4$ @inulin nanocomposite is 40.21 emu/g, which is 34% lower than that of  $\text{Fe}_3\text{O}_4$  nanoparticles. This lower saturation is due to the presence of non-magnetic inulin, i.e., inulin, in the structure of the synthesized composite. However, this slight decrease in the magnetic saturation is reasonable, and the nanocomposite can still be removed from the reaction solution efficiently by applying an external magnetic field or a simple magnet.

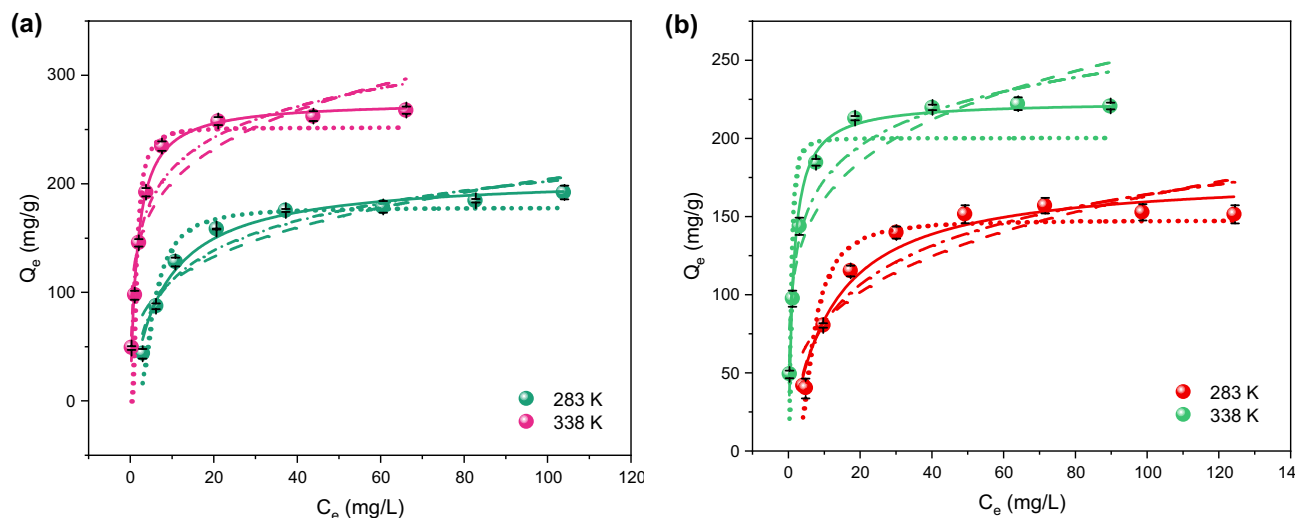
**Effect of operating conditions.** The adsorption experiments were performed at different pHs (1–11) to find the best solution pH for each dye. The other operating factors were constant, including the temperature of 25 °C, the adsorbent dosage of 0.5 g/L, the dye concentration of 25 mg/L, and the adsorption time of 180 min. As known, molecular aggregation occurs in aqueous solutions when the pH value is very low, resulting in considerable aggregates; thus, it is reasonable to detect the optimum pH for every solution. Figure 4a shows the removal efficiency of both dyes at different solution pHs. The maximum adsorption rates of about 95% and 91% were obtained at a pH of 5 and 7 for MO and CV dyes, respectively. Such adsorption trends by pH variation can be explained by the  $\text{pH}_{\text{ZPC}}$  curve, reported in Fig. 3b. The solution pH affects the net surface for amphoteric molecules containing both negative and positive charges. They become more positively or negatively charged by either gaining or losing protons. Because MO acts as a cationic dye in highly acidic solutions<sup>36</sup>, its removal efficiency is lower due to the electrostatic repulsion between cationic dye and negatively charged adsorbent surface. By further increasing the solution pH, the number of positive charges is reduced, achieving the maximum MO removal efficiency at pH 5. However, at a pH higher than 5, the excessive quantity of hydroxyl ions competing with MO molecules for adsorption sites and electrostatic repulsion will reduce its adsorption rate. Moreover, the color of the solution containing MO dye becomes shallow, not only because of the change in pH but also due to the association with the adsorption by the  $\text{Fe}_3\text{O}_4$ @inulin adsorbent. For CV adsorption, lower removal efficiency at an acidic pH might be due to excessive  $\text{H}^+$  ions competing with CV dye cations for the adsorption sites<sup>37</sup>. Under a pH higher than the neutral solution, the CV removal efficiency does not change significantly. Therefore, the optimal pH value for CV removal was found to be 7.

Figure 4b exhibits the effect of  $\text{Fe}_3\text{O}_4$ @inulin adsorbent dosage on the removal efficiency of both dyes under different concentrations in the range of 0.1–0.8 g/L. The optimal solution pH related to each dye was considered in this case study. The removal efficiencies by 0.5 g/L concentration of adsorbent are about 6.3 and 9.1 times when the adsorbent dosage is 0.1 g/L for MO and CV adsorption, respectively. This significant increment is due to the enhanced active functional groups and increased number of active binding sites in the nanocomposite. At dosages higher than 0.5 g/L, the removal efficiency increases insignificantly because of the saturation of adsorption sites. Hence, the optimum amount of adsorbent for adsorbing both dyes is selected as 0.5 g/L for the following examinations.

**Adsorption isotherms.** Adsorption isotherm models can achieve the equilibrium relations between the adsorbate and adsorbent. To estimate the adsorption behavior of the prepared nanocomposite, four non-linear isotherm models, Langmuir, Freundlich, Dubinin–Radushkevich (D–R), Temkin utilized, and their correlations are given below<sup>38</sup>:

$$\text{Langmuir: } Q_e = \frac{Q_m K_L C_e}{1 + K_L C_e} \quad (3)$$





**Figure 5.** Isotherm curves under different temperatures for (a) MO adsorption at pH of 5 and (b) CV adsorption at pH of 7; solid lines: Langmuir, dashed lines: Freundlich, dotted lines: Dubinin-Radushkevich, dash-dotted lines: Temkin.

$$\text{Freundlich: } Q_e = K_F C_e^{\frac{1}{n}} \quad (4)$$

$$\text{Dubinin-Radushkevich: } Q_e = Q_m \exp \left( -K_D \left( RT \ln \left( 1 + \frac{1}{C_e} \right) \right)^2 \right) \quad (5)$$

$$\text{Temkin: } Q_e = \frac{RT}{B_T} \ln(K_T C_e) \quad (6)$$

where  $Q_e$  is the amount of dye adsorbed at the equilibrium state,  $Q_m$  is the Langmuir monolayer adsorption capacity,  $K_L$  is the Langmuir isotherm constant,  $K_F$  is the Freundlich isotherm constant, and  $n$  is the Freundlich exponent<sup>39</sup>. The term  $K_D$  is the isotherm constant in the thermodynamic equilibrium constant in the adsorption process,  $R$  is the gas constant (8.314 J/mol K), and  $T$  is the temperature. Also, the terms  $K_T$  and  $B_T$  are the Temkin isotherm constant and a constant related to the heat of adsorption, respectively. The Langmuir isotherm is typically utilized when there is ideal monolayer adsorption on a homogeneous surface. The Freundlich isotherm is generally appropriate for nonideal adsorption on heterogeneous surfaces. The Freundlich isotherm is a purely empirical model, presuming that a great number and a variety of existing sites act simultaneously, each with a different free energy of sorption. The D-R model assumes that the adsorption equilibrium relation for a specific adsorbent-adsorbate combination can be expressed by the adsorption potential independent of temperature. The Temkin isotherm model presumes that the adsorption heat of all molecules is linearly reduced with the increment in coverage of the adsorbent surface and that adsorption is described by a uniform distribution of binding energies<sup>40</sup>.

The isotherm modeling of MO and CV adsorption onto the  $\text{Fe}_3\text{O}_4$ @inulin composite is illustrated in Fig. 5 for two temperatures of 283 and 338 K. The results and fitting parameters related to all isotherm models at other temperatures within this range are reported in Table 1. In this study, the adsorbent dosage and adsorption time are 0.5 g/L and 180 min, respectively. At all temperatures, the Langmuir isotherm model exhibited a better prediction for the adsorption data related to both dyes due to a coefficient of determination ( $R^2$ ) higher than 0.98 and the minimum reduced chi-squared value among all considered models. The temperature rise leads to an increase in the adsorption capacity of the nanocomposite, indicating that higher temperatures favor the MO and CV adsorption process because of its endothermic nature. Also, in the Freundlich isotherm model, the constant ( $K_F$ ) value is higher at elevated temperatures, further demonstrating that the adsorption process is endothermic. This increment in adsorption rate can be explained by the temperature-induced breakage of some internal bonds at the composite active surface, leading to an enhanced number of adsorption sites, as well as the dye molecule diffusion into the composite surface cavities raised by a temperature trigger. Additionally, the values of  $1/n$  in the Freundlich models at all temperatures are smaller than 1, demonstrating a favorable adsorption process.

**Adsorption kinetics.** Kinetics investigation for the pollutant adsorption from contaminated water can be worthwhile because it enables finding the adsorption equilibrium time, adsorption kinetics rate, and the adsorbate concentration in each phase after achieving the equilibrium state. Here, pseudo-first-order (PFO), pseudo-second-order (PSO), and Elovich kinetics models are used to better examine the adsorption mechanism of MO and CV dyes onto the  $\text{Fe}_3\text{O}_4$ @inulin nanocomposite.

Model	Dye	MO				CV			
	Temperature [K]	283	298	318	338	283	298	318	338
Langmuir	$K_L$ [L/mg]	0.1289	0.2296	0.2869	0.6137	0.0902	0.1586	0.3079	0.7581
	$Q_m$ [mg/g]	207.42	223.64	255.23	276.26	177.14	192.88	209.95	223.74
	Reduced chi-squared	59.749	49.023	36.121	52.880	83.947	46.669	17.638	85.860
	$R^2$	0.9819	0.9888	0.9941	0.9934	0.9683	0.9868	0.9962	0.9860
	Adjusted $R^2$	0.9789	0.9870	0.9931	0.9923	0.9638	0.9849	0.9957	0.9840
Freundlich	$K_F$ [(mg/g)(L/mg) <sup>1/n</sup> ]	59.477	79.173	93.948	125.571	41.901	57.730	77.454	102.27
	$n$ [dimensionless]	3.732	4.198	4.184	4.872	3.384	3.829	4.353	5.061
	Reduced chi-squared	471.78	414.04	764.35	1184.01	452.68	528.32	699.24	693.89
	$R^2$	0.8572	0.9069	0.8759	0.8523	0.8296	0.8508	0.8621	0.8869
	Adjusted $R^2$	0.8334	0.8902	0.8552	0.8277	0.8062	0.8296	0.8310	0.8708
Dubinin–Radushkevich	$K_D$	4.8122	2.1686	1.2620	3.1610	6.9059	2.0001	5.5347	1.0984
	$Q_m$	178.47	199.62	228.64	251.93	147.84	164.55	184.23	200.33
	Reduced chi-squared	233.84	666.68	605.74	730.41	186.25	418.77	516.45	966.34
	$R^2$	0.9292	0.8484	0.9016	0.9089	0.9298	0.8817	0.8907	0.8425
	Adjusted $R^2$	0.9174	0.8232	0.8852	0.8937	0.9198	0.8648	0.8751	0.8200
Temkin	$B_T$	59.182	66.753	61.144	67.504	66.476	70.141	75.979	88.877
	$K_T$	1.6319	4.8942	5.3783	16.962	0.9660	2.2236	5.5592	24.041
	Reduced chi-squared	218.68	138.69	289.24	492.37	220.70	235.52	297.04	229.57
	$R^2$	0.9338	0.9684	0.9530	0.9386	0.9169	0.9335	0.9371	0.9626
	Adjusted $R^2$	0.9227	0.9632	0.9452	0.9283	0.9050	0.9240	0.9281	0.9572

**Table 1.** Fitting parameters obtained from isotherm models for the MO and CV adsorption onto the Fe<sub>3</sub>O<sub>4</sub>@inulin nanocomposite.

The PFO model assumes that the rate of variation in solute adsorption is directly proportional to the difference in saturated concentration and the amount of adsorptive solid adsorbed over time. The PSO kinetics describes that the adsorption rate is measured by the interaction between the adsorbate and adsorbent species. The Elovich model can estimate the surface and mass diffusion, activation and deactivation energy of the adsorption system. In this model, the adsorption rate of solute is exponentially reduced by increasing the adsorbed solute amount<sup>41</sup>. The non-linear equations of these models are as follows<sup>42</sup>:

$$\text{PFO: } Q_t = Q_e(1 - \exp(-k_1 t)) \quad (7)$$

$$\text{PSO: } Q_t = \frac{k_2 Q_e^2 t}{1 + Q_e k_2 t} \quad (8)$$

$$\text{Elovich: } Q_t = \frac{1}{\beta} \ln(\alpha \beta t + 1) \quad (9)$$

where  $Q_t$  is the amount of dye adsorbed at time  $t$ , and the terms  $k_1$  and  $k_2$  are the rate constants for PFO and PSO models, respectively. Also, the terms  $Q_e$  and  $\beta$  are the initial adsorption rate and the desorption constant in the Elovich model, respectively. The fitting results of kinetic data are shown in Fig. 6. Among these three models, the PSO model provides excellent predictions of the experimental kinetics data of the adsorption capacity of the prepared nanocomposite for both dyes. Table 2 presents the parameters resulting from fitting the kinetics models to the experimental data. The highest  $R^2$  and lowest reduced chi-squared values confirm that the adsorption mechanism can be characterized by a PSO kinetics model. The applicability of this model implies that the adsorption of both dyes onto the Fe<sub>3</sub>O<sub>4</sub>@inulin adsorbent surface is a chemisorption process<sup>43</sup>, where the molecules of dyes have been bounded to the Fe<sub>3</sub>O<sub>4</sub>@inulin through surface exchange reactions. The dye adsorption mechanism by the prepared Fe<sub>3</sub>O<sub>4</sub>@inulin nanocomposite is also shown in Fig. 6b. The most contributive forces are electrostatic attraction and hydrogen bonding interactions (dipole–dipole and Yoshida). The contribution of each force in dye adsorption differs at different pHs, as its details are reported in the literature<sup>44</sup>.

**Thermodynamic study.** The thermodynamic parameters of the enthalpy ( $\Delta H^\circ$ ), entropy ( $\Delta S^\circ$ ), and Gibbs free energy ( $\Delta G^\circ$ ) were measured by the following correlations:

$$K_c = \frac{Q_e}{C_e} \quad (10)$$

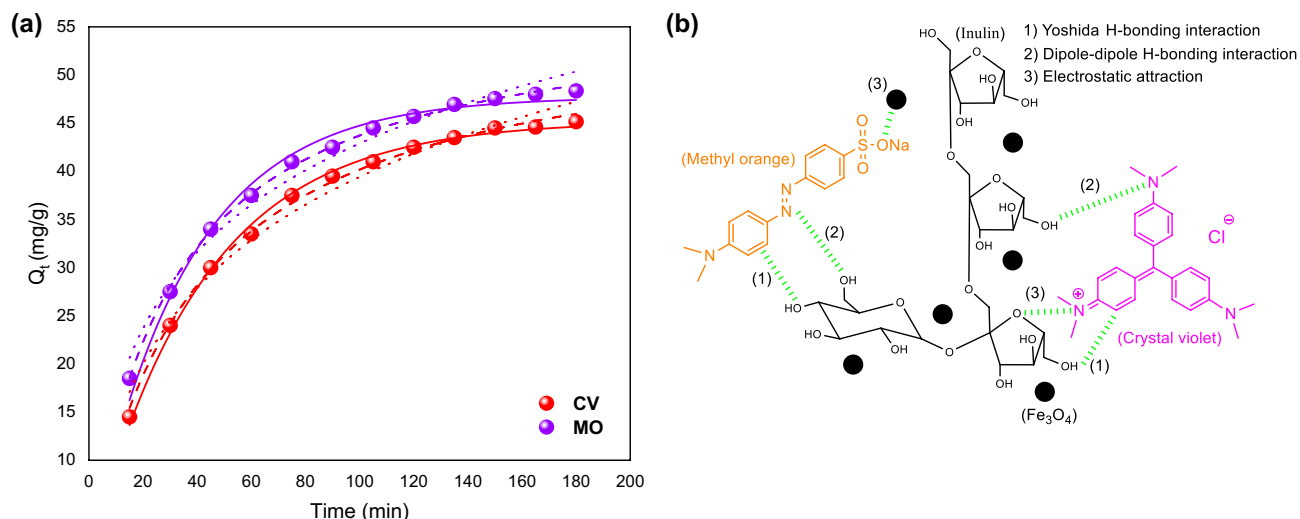


**Figure 6.** (a) Kinetics data of MO and CV adsorption process at their optimum solution pH predicted by non-linear kinetics models at  $C_a = 0.5$  g/L and  $C_{dye} = 25$  mg/L: solid line: PFO, dashed line: PSO, dotted line: Elovich; (b) proposed mechanism of dye adsorption onto the  $Fe_3O_4$ @inulin nanocomposite.

Parameter	Dye	
	MO	CV
<b>PFO</b>		
$Q_e$	47.736	45.243
$k_1$ [ $\text{min}^{-1}$ ]	0.0276	0.0239
Reduced chi-squared	1.148	0.3634
$R^2$	0.9880	0.9964
Adjusted $R^2$	0.9868	0.9960
<b>PSO</b>		
$Q_e$	57.523	56.094
$k_2$ [ $\text{g mg}^{-1} \text{min}^{-1}$ ]	5.501	4.497
Reduced chi-squared	0.1265	0.3192
$R^2$	0.9986	0.9968
Adjusted $R^2$	0.9985	0.9965
<b>Elovich</b>		
$\alpha$ [ $\text{mg/g min}$ ]	3.344	2.233
$\beta$	0.0764	0.0719
Reduced chi-squared	1.7776	2.0849
$R^2$	0.9814	0.9793
Adjusted $R^2$	0.9796	0.9773

**Table 2.** Fitting parameters obtained from kinetics models for MO and CV adsorption onto the  $Fe_3O_4$ @inulin nanocomposite.

$$\Delta G^\circ = -RT \ln K_c \quad (11)$$

$$\ln K_c = -\frac{\Delta H^\circ}{RT} + \frac{\Delta S^\circ}{R} \quad (12)$$

where  $K_c$  is the adsorption equilibrium constant. The thermodynamic data calculated from the above equations are reported in Table 3. The positive value of  $\Delta H^\circ$  proposed that the adsorption process was endothermic, which agreed with the increasing dye adsorption with temperature. The  $\Delta G^\circ$  with negative values indicated a spontaneous adsorption process. The  $\Delta G^\circ$  is reduced by increasing temperature, proposing that the adsorption process is more favorable at higher temperatures. Additionally, the  $\Delta S^\circ$  with positive quantities demonstrated enhanced randomness at the solution-solid interface because of several structural changes throughout the process. The surface of the composites and dye molecules in the aqueous solution was surrounded by hydration layers of

Dye/parameter	$\Delta H^\circ$ [kJ/mol] at 298 K	$\Delta S^\circ$ [kJ/mol K] at 298 K	$\Delta G^\circ$ [kJ/mol]			
			283 K	298 K	313 K	338 K
MO	11.5448	46.0172	-1.4519	-2.1345	-2.9897	-3.9379
CV	10.2271	37.8977	-0.4691	-1.0695	-1.7101	-2.5345

**Table 3.** Thermodynamic parameters for CO<sub>2</sub> adsorption onto Fe<sub>3</sub>O<sub>4</sub>@inulin nanocomposite.

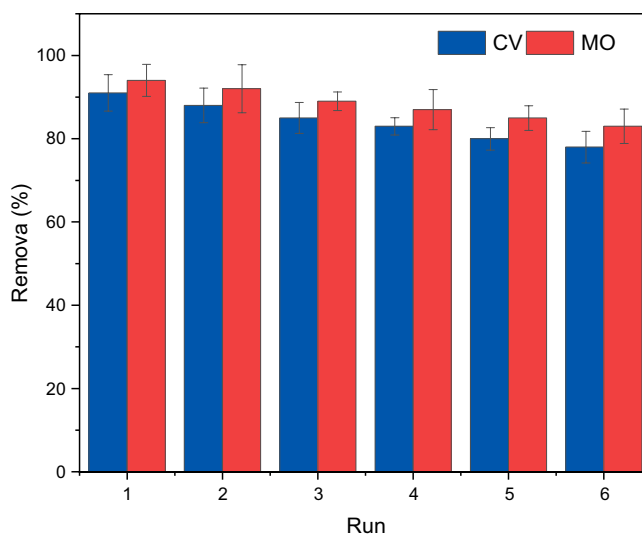


**Figure 7.** Adsorbent reusability for MO and CV adsorption by Fe<sub>3</sub>O<sub>4</sub>@inulin in terms of removal efficiency; T = 298 K, pH = 7 for CV and 5 for MO, C<sub>a</sub> = 0.5 g/L, C<sub>dye</sub> = 25 mg/L, t = 180 min.

water molecules. Throughout the adsorption process, the water molecules ordered in these hydration layers were disturbed and compelled, improving the degree of freedom in the adsorbent-dye interaction.

**Adsorbent reusability.** In addition to acceptable adsorption performance, easy reusability and multi-cycle utilization are critical factors in providing a feasible, scalable and efficient treatment system because it influences the adsorbent performance and reduces the operational cost. The ethanol and acetone with high dipole moments were harnessed as the desorption agents to regenerate the adsorbent. First, dye particles were adsorbed onto the Fe<sub>3</sub>O<sub>4</sub>@inulin. After the adsorption process, the dye-loaded particles of the adsorbent were regenerated via ethanol or acetone, exhaustively washed with DI water and then used for dye adsorption again. The Fe<sub>3</sub>O<sub>4</sub>@inulin was reused six times to check its applicability in removing MO and CV dyes. The reusability results for the adsorption of both dyes are reported in Fig. 7 under their optimum solution pH and adsorbent dosage. Notably, the removal efficiency of Fe<sub>3</sub>O<sub>4</sub>@inulin magnetic composite decreases from 94.92 to 83.34% and 91.13–78.86% after six successive adsorption cycles for MO and CV dyes, respectively, maintaining more than 87% of their initial adsorption rates. The decrease in the adsorption performance with increasing cycle number might be due to the saturation of sorption sites by strongly adsorbed dye molecules. The Fe<sub>3</sub>O<sub>4</sub>@inulin exhibits high MO and CV removal rates with excellent reusability.

Even though each sorbent has unique nature, intrinsic characteristics, advantages, and disadvantages, the adsorption capacity of the Fe<sub>3</sub>O<sub>4</sub>@inulin for MO and CV removal is compared with other bio-nano adsorbents. Table 4 compares different bio-adsorbents at their optimal solution pH. The best solution pH, isotherm and kinetics models are listed as well. As shown, the capacity of magnetized inulin is higher than that of similar magnetized biomaterials in removing both dyes. Such a performance approves that the Fe<sub>3</sub>O<sub>4</sub>@inulin is an excellent magnetized sorbent with good stability for adsorption of both anionic and cationic dyes under an appropriate solution pH.

## Conclusion

Nowadays, dye-contaminated water has become a severe environmental concern due to growing industrialization worldwide. Thus, environmentalists and researchers should urgently consider developing efficient methods and materials to mitigate such problems. In this work, we synthesized a new bio-nano adsorbent, i.e., magnetized inulin with Fe<sub>3</sub>O<sub>4</sub>, to remove toxic anionic and cationic dyes from wastewater. Various physical and structural analyses were conducted to evaluate the fabrication of the magnetic nanocomposite. According to the FTIR spectra, the presence of the Fe–O bond approved the successful synthesis of Fe<sub>3</sub>O<sub>4</sub>@inulin with an average crystalline size of 10.9 nm obtained from its XRD pattern. The SEM–EDX results demonstrated a relatively uniform,

Adsorbent	Dye	Solution pH	Isotherm model	Kinetics model	$Q_m$ [mg/g]	Reusability (cycle and reduction in removal efficiency)	References
Chitosan microspheres	MO	3.1	Langmuir	PSO	207	5 and ~9%	45
Modified gum Tragacanth/graphene oxide	CV	8	Langmuir	PSO	94.0	3 and ~15%	46
Magnetic lignin-based carbon nanoparticles	MO	5	Langmuir	PSO	113.0	4 & 10%	47
Magnetic starch-graft-poly(acrylic acid) hydrogels	CV	7	Langmuir	PSO	80.64	5 and ~5%	48
Layered double hydroxides@Fe <sub>3</sub> O <sub>4</sub> /PVA	MO	6	Freundlich	PSO	19.59	4 and 50%	49
Magnetic kappa-carrageenan nanocomposite beads	CV	8	Langmuir	PSO	84.7		50
Xanthan gum/PVI hydrogel	CV	7	Langmuir	PFO	453.0		51
Ferric oxide-biochar nanocomposites	MO	8	Freundlich	PSO	20.53		52
Modified cellulose with glycidyl methacrylate	CV	9	Langmuir	PSO	218.8	8 and ~30	53
Chitosan/organic rectorite composite	MO	3	Langmuir	PSO	5.56		54
Hydroxyapatite nanoparticles impregnated magnetic bentonite	CV	8	Freundlich	PSO	1290.30	5 and ~5%	55
Fe <sub>3</sub> O <sub>4</sub> @inulin	MO	5	Langmuir	PSO	276.26	6 and ~11%	This work
	CV	7	Langmuir	PSO	223.57	6 and ~12%	

**Table 4.** Performance comparison of different bio-nano adsorbents for treating water contaminated with MO and CV dyes. PVA: ed poly (vinyl alcohol), PVI: poly (N-vinyl imidazole).

regular dispersion of spherical nanoparticles ranging from 10 to 20 nm on the composite surface. Based on the BET analysis, the adsorbent's specific surface area, pore volume, and average pore diameter were 66.15 m<sup>2</sup>/g, 0.181 cm<sup>3</sup>/g, and 11.027 nm, respectively. The VSM analysis showed that the nanocomposite's magnetic saturation, i.e., 40.21 emu/g, was about 34% lower than that for pure Fe<sub>3</sub>O<sub>4</sub> nanoparticles. Considering the pH<sub>PZC</sub> value of 6 and the anionic and cationic characteristics of both dyes, the optimal solution pH was 5 for MO and 7 for CV. According to the highest R<sup>2</sup> value (>0.99) and the lowest reduced chi-squared, the Langmuir isotherm fitted better the experimental data with a maximum adsorption capacity of 276.26 mg/g for MO and 223.57 mg/g for CV at 338 K. Considering these statistical criteria, the pseudo-second-order model (R<sup>2</sup>>0.99 and reduced chi-squared <1) was a better kinetics model than pseudo-second-order and Elovich models in predicting the kinetics data of both dyes. In addition, the thermodynamic parameter demonstrated that the dye adsorption by Fe<sub>3</sub>O<sub>4</sub>@inulin was an endothermic and spontaneous process. Furthermore, after using the adsorbent six times, its removal efficiency maintained more than 87% of its initial adsorption rate for both pollutants, exhibiting excellent stability and reusability of the prepared nanocomposite. Overall, the comparison of the ability of different magnetized adsorbents in adsorbing cationic and anionic dyes verified that the Fe<sub>3</sub>O<sub>4</sub>@inulin could be a promising candidate for treating water contaminated with toxic dyes.

### Data availability

Data are available with the permission of [Prof. Ali Maleki]. The data that support the findings of this study are available from the corresponding authors, [Prof. Ali Maleki and Prof. Zhenjiang You], upon reasonable request.

Received: 15 September 2022; Accepted: 19 December 2022

Published online: 20 December 2022

### References

- Liang, L. *et al.* Review of organic and inorganic pollutants removal by biochar and biochar-based composites. *Biochar* **3**, 255–281 (2021).
- Behroozi, A. H. & Ataabadi, M. R. Improvement in microfiltration process of oily wastewater: A comprehensive review over two decades. *J. Environ. Chem. Eng.* **9**, 104981 (2021).
- Khajavian, M., Salehi, E. & Vatanpour, V. Chitosan/polyvinyl alcohol thin membrane adsorbents modified with zeolitic imidazolate framework (ZIF-8) nanostructures: Batch adsorption and optimization. *Sep. Purif. Technol.* **241**, 116759 (2020).
- Piri, F., Mollahosseini, A. & Hosseini, M. M. Enhanced adsorption of dyes on microwave-assisted synthesized magnetic zeolite-hydroxyapatite nanocomposite. *J. Environ. Chem. Eng.* **7**, 103338 (2019).
- Al-Ansari, M. M., Li, Z., Masood, A. & Rajaselvam, J. Decolorization of azo dye using a batch bioreactor by an indigenous bacterium *Enterobacter aerogenes* ES014 from the waste water dye effluent and toxicity analysis. *Environ. Res.* **205**, 112189 (2022).
- Ahmed, D. N., Naji, L. A., Faisal, A. A., Al-Ansari, N. & Naushad, M. Waste foundry sand/MgFe-layered double hydroxides composite material for efficient removal of Congo red dye from aqueous solution. *Sci. Rep.* **10**, 1–12 (2020).
- Koohi, P., Rahbar-kelishami, A. & Shayesteh, H. Efficient removal of congo red dye using Fe<sub>3</sub>O<sub>4</sub>/NiO nanocomposite: Synthesis and characterization. *Environ. Technol. Innov.* **23**, 101559 (2021).
- Peter, C. *et al.* N-doped ZnO/graphene oxide: A photostable photocatalyst for improved mineralization and photodegradation of organic dye under visible light. *Ionics* **25**, 327–339 (2019).
- Maleki, A. *et al.* Investigation of potato peel-based bio-sorbent efficiency in reactive dye removal: Artificial neural network modeling and genetic algorithms optimization. *J. Adv. Environ. Health Res.* **1**, 21–28 (2013).
- Moradihamedani, P. Recent advances in dye removal from wastewater by membrane technology: A review. *Polym. Bull.* **79**, 2603–2631 (2021).

11. Ghanbari, F. & Moradi, M. A comparative study of electrocoagulation, electrochemical Fenton, electro-Fenton and peroxi-coagulation for decolorization of real textile wastewater: Electrical energy consumption and biodegradability improvement. *J. Environ. Chem. Eng.* **3**, 499–506 (2015).
12. Xu, S. *et al.* Influence of output current on decolorization efficiency of azo dye wastewater by a series system with multi-stage reverse electro dialysis reactors. *Energy Convers. Manag.* **228**, 113639 (2021).
13. Basith, M., Ahsan, R., Zarin, I. & Jalil, M. Enhanced photocatalytic dye degradation and hydrogen production ability of Bi<sub>2</sub>FeO<sub>4</sub>-rGO nanocomposite and mechanism insight. *Sci. Rep.* **8**, 1–11 (2018).
14. Nguyen, D. L. T. *et al.* Metal salt-modified biochars derived from agro-waste for effective congo red dye removal. *Environ. Res.* **200**, 111492 (2021).
15. Rodrigues, C. S., Madeira, L. M. & Boaventura, R. A. Synthetic textile dyeing wastewater treatment by integration of advanced oxidation and biological processes—Performance analysis with costs reduction. *J. Environ. Chem. Eng.* **2**, 1027–1039 (2014).
16. Wong, S. *et al.* Effective removal of anionic textile dyes using adsorbent synthesized from coffee waste. *Sci. Rep.* **10**, 1–13 (2020).
17. Bayomie, O. S. *et al.* Novel approach for effective removal of methylene blue dye from water using fava bean peel waste. *Sci. Rep.* **10**, 1–10 (2020).
18. Ali, F., Khan, S. B., Kamal, T., Alamry, K. A. & Asiri, A. M. Chitosan-titanium oxide fibers supported zero-valent nanoparticles: Highly efficient and easily retrievable catalyst for the removal of organic pollutants. *Sci. Rep.* **8**, 1–18 (2018).
19. Jawad, A. H., Mubarak, N. S. A. & Abdulhameed, A. S. Hybrid crosslinked chitosan-epichlorohydrin/TiO<sub>2</sub> nanocomposite for reactive red 120 dye adsorption: Kinetic, isotherm, thermodynamic, and mechanism study. *J. Polym. Environ.* **28**, 624–637 (2020).
20. Reghioia, A. *et al.* Magnetic chitosan-glutaraldehyde/zinc oxide/Fe<sub>3</sub>O<sub>4</sub> nanocomposite: Optimization and adsorptive mechanism of remazol brilliant blue R dye removal. *J. Polym. Environ.* **29**, 3932–3947 (2021).
21. Kazemi, J. & Javanbakht, V. Alginate beads impregnated with magnetic Chitosan@ Zeolite nanocomposite for cationic methylene blue dye removal from aqueous solution. *Int. J. Biol. Macromol.* **154**, 1426–1437 (2020).
22. Al-Musawi, T. J., Mengelizadeh, N., Al Rawi, O. & Balarak, D. Capacity and modeling of acid blue 113 dye adsorption onto chitosan magnetized by Fe<sub>2</sub>O<sub>3</sub> nanoparticles. *J. Polym. Environ.* **30**, 344–359 (2022).
23. Tanhaei, B., Ayati, A., Iakovleva, E. & Sillanpää, M. Efficient carbon interlayered magnetic chitosan adsorbent for anionic dye removal: Synthesis, characterization and adsorption study. *Int. J. Biol. Macromol.* **164**, 3621–3631 (2020).
24. de Figueiredo Neves, T. *et al.* Novel magnetic chitosan/quaternary ammonium salt graphene oxide composite applied to dye removal. *J. Environ. Chem. Eng.* **8**, 103820 (2020).
25. Hernández-Martínez, A. R. *et al.* Evaluation of inulin replacing chitosan in a polyurethane/polysaccharide material for Pb<sup>2+</sup> removal. *Molecules* **22**, 2093 (2017).
26. Qi, X. *et al.* Recent advances in polysaccharide-based adsorbents for wastewater treatment. *J. Clean. Prod.* **315**, 128221 (2021).
27. Gaio, I. *et al.* Liquefied petroleum gas as solvent medium for the treatment of immobilized pectinases. *Biocatal. Agric. Biotechnol.* **11**, 108–115 (2017).
28. Sirajudheen, P., Nikitha, M. R., Karthikeyan, P. & Meenakshi, S. Perceptive removal of toxic azo dyes from water using magnetic Fe<sub>3</sub>O<sub>4</sub> reinforced graphene oxide-carboxymethyl cellulose recyclable composite: Adsorption investigation of parametric studies and their mechanisms. *Surf. Interfaces* **21**, 100648 (2020).
29. Bateni, A., Valizadeh, K., Salahshour, Y., Behroozi, A. H. & Maleki, A. Fabrication and characterization of pectin-graphene oxide-magnesium ferrite-zinc oxide nanocomposite for photocatalytic degradation of diclofenac in an aqueous solution under visible light irradiation. *J. Environ. Manag.* **324**, 116358 (2022).
30. Fashi, F., Ghaemi, A. & Behroozi, A. H. Piperazine impregnation on Zeolite 13X as a novel adsorbent for CO<sub>2</sub> capture: Experimental and modeling. *Chem. Eng. Commun.* **208**, 1104–1120 (2021).
31. Vatanpour, V. *et al.* Investigation of boron nitride/silver/graphene oxide nanocomposite on separation and antibacterial improvement of polyethersulfone membranes in wastewater treatment. *J. Environ. Chem. Eng.* **10**, 107035 (2022).
32. Maleki, A., Hassanzadeh-Afrouzi, F., Varzi, Z. & Esmaeili, M. S. Magnetic dextrin nanobiomaterial: an organic-inorganic hybrid catalyst for the synthesis of biologically active polyhydroquinoline derivatives by asymmetric Hantzsch reaction. *Mater. Sci. Eng., C* **109**, 110502 (2020).
33. Rani, N. *et al.* X-ray analysis of MgO nanoparticles by modified Scherer's Williamson-Hall and size-strain method. *Mater. Today Proc.* **12**, 543–548 (2019).
34. Rahman, M. M., Muttakin, M., Pal, A., Shafiullah, A. Z. & Saha, B. B. A statistical approach to determine optimal models for IUPAC-classified adsorption isotherms. *Energies* **12**, 4565 (2019).
35. Kayan, A. Inorganic-organic hybrid materials and their adsorbent properties. *Adv. Compos. Hybrid Mater.* **2**, 34–45 (2019).
36. El Naga, A. O. A., Shaban, S. A. & El Kady, F. Y. Metal organic framework-derived nitrogen-doped nanoporous carbon as an efficient adsorbent for methyl orange removal from aqueous solution. *J. Taiwan Inst. Chem. Eng.* **93**, 363–373 (2018).
37. Purkait, M. K., Maiti, A., DasGupta, S. & De, S. Removal of congo red using activated carbon and its regeneration. *J. Hazard. Mater.* **145**, 287–295. <https://doi.org/10.1016/j.jhazmat.2006.11.021> (2007).
38. Kamran, U., Bhatti, H. N., Noreen, S., Tahir, M. A. & Park, S.-J. Chemically modified sugarcane bagasse-based biocomposites for efficient removal of acid red 1 dye: Kinetics, isotherms, thermodynamics, and desorption studies. *Chemosphere* **291**, 132796 (2022).
39. Ghaemi, A. & Behroozi, A. H. Comparison of hydroxide-based adsorbents of Mg(OH)<sub>2</sub> and Ca(OH)<sub>2</sub> for CO<sub>2</sub> capture: Utilization of response surface methodology, kinetic, and isotherm modeling. *Greenhouse Gases Sci. Technol.* **10**, 948–964 (2020).
40. Maryanti, R., Nandiyanto, A. B. D., Manullang, T. I. B., Hafid, A. & Sunardi, S. Adsorption of dye on carbon microparticles: Physicochemical properties during adsorption, adsorption isotherm and education for students with special needs. *Sains Malays.* **49**, 2949–2960 (2020).
41. Jain, N. & Maiti, A. Fe–Mn–Al metal oxides/oxyhydroxides as As(III) oxidant under visible light and adsorption of total arsenic in the groundwater environment. *Sep. Purif. Technol.* **302**, 122170 (2022).
42. Nakarmi, K. J. *et al.* Synthesis of biochar from iron-free and iron-containing microalgal biomass for the removal of pharmaceuticals from water. *Environ. Res.* **214**, 114041. <https://doi.org/10.1016/j.envres.2022.114041> (2022).
43. Mittal, H., Al Alili, A., Morajkar, P. P. & Alhassan, S. M. Graphene oxide crosslinked hydrogel nanocomposites of xanthan gum for the adsorption of crystal violet dye. *J. Mol. Liq.* **323**, 115034 (2021).
44. George, G. & Saravanakumar, M. P. Facile synthesis of carbon-coated layered double hydroxide and its comparative characterisation with Zn–Al LDH: application on crystal violet and malachite green dye adsorption—Isotherm, kinetics and Box-Behnken design. *Environ. Sci. Pollut. Res.* **25**, 30236–30254 (2018).
45. Zhai, L., Bai, Z., Zhu, Y., Wang, B. & Luo, W. Fabrication of chitosan microspheres for efficient adsorption of methyl orange. *Chin. J. Chem. Eng.* **26**, 657–666 (2018).
46. Sahraei, R., Pour, Z. S. & Ghaemy, M. Novel magnetic bio-sorbent hydrogel beads based on modified gum tragacanth/graphene oxide: Removal of heavy metals and dyes from water. *J. Clean. Prod.* **142**, 2973–2984 (2017).
47. Ma, Y.-Z., Zheng, D.-F., Mo, Z.-Y., Dong, R.-J. & Qiu, X.-Q. Magnetic lignin-based carbon nanoparticles and the adsorption for removal of methyl orange. *Colloids Surf., A* **559**, 226–234 (2018).
48. Pourjavadi, A., Hosseini, S. H., Seidi, F. & Soleyman, R. Magnetic removal of crystal violet from aqueous solutions using polysaccharide-based magnetic nanocomposite hydrogels. *Polym. Int.* **62**, 1038–1044 (2013).
49. Mallakpour, S. & Hatami, M. An effective, low-cost and recyclable bio-adsorbent having amino acid intercalated LDH@ Fe<sub>3</sub>O<sub>4</sub>/PVA magnetic nanocomposites for removal of methyl orange from aqueous solution. *Appl. Clay Sci.* **174**, 127–137 (2019).



50. Mahdavinia, G. R., Iravani, S., Zoroufi, S. & Hosseinzadeh, H. Magnetic and K<sup>+</sup>-cross-linked kappa-carrageenan nanocomposite beads and adsorption of crystal violet. *Iran. Polym. J.* **23**, 335–344 (2014).
51. Mohamed, R. R., Abu Elella, M. H., Sabaa, M. W. & Saad, G. R. Synthesis of an efficient adsorbent hydrogel based on biodegradable polymers for removing crystal violet dye from aqueous solution. *Cellulose* **25**, 6513–6529 (2018).
52. Chaukura, N., Murimba, E. C. & Gwenzi, W. Synthesis, characterisation and methyl orange adsorption capacity of ferric oxide—Biochar nano-composites derived from pulp and paper sludge. *Appl. Water Sci.* **7**, 2175–2186 (2017).
53. Zhou, Y. *et al.* Removal of crystal violet by a novel cellulose-based adsorbent: Comparison with native cellulose. *Ind. Eng. Chem. Res.* **53**, 5498–5506 (2014).
54. Zeng, L. *et al.* Chitosan/organic rectorite composite for the magnetic uptake of methylene blue and methyl orange. *Carbohydr. Polym.* **123**, 89–98 (2015).
55. Ain, Q. U. *et al.* Facile fabrication of hydroxyapatite-magnetite-bentonite composite for efficient adsorption of Pb(II), Cd(II), and crystal violet from aqueous solution. *J. Clean. Prod.* **247**, 119088 (2020).

### Author contributions

K.V.: Funding Acquisition, Formal Analysis, Data Interpretation, Investigation. A.B.: Data curation, Investigation, Formal Analysis, Data Interpretation. N.S.: Data curation, Investigation, Formal Analysis, Data Interpretation. M.R.A.: Investigation, Data Interpretation, Methodology, Graphics, Writing—Original Draft. A.H.B.: Conceptualization, Methodology, Project Administration, Research Design, Data Interpretation, Investigation, Writing—Original Draft, Writing—Review & Editing. A.M.: Corresponding author, Supervision, Conceptualization, Methodology, Resources, Research Design, Project Administration, Writing—Review & Editing. Z.Y.: Corresponding author, Supervision, Conceptualization, Writing—Review & Editing.

### Competing interests

The authors declare no competing interests.

### Additional information

**Supplementary Information** The online version contains supplementary material available at <https://doi.org/10.1038/s41598-022-26652-7>.

**Correspondence** and requests for materials should be addressed to A.M. or Z.Y.

**Reprints and permissions information** is available at [www.nature.com/reprints](http://www.nature.com/reprints).

**Publisher's note** Springer Nature remains neutral with regard to jurisdictional claims in published maps and institutional affiliations.



**Open Access** This article is licensed under a Creative Commons Attribution 4.0 International License, which permits use, sharing, adaptation, distribution and reproduction in any medium or format, as long as you give appropriate credit to the original author(s) and the source, provide a link to the Creative Commons licence, and indicate if changes were made. The images or other third party material in this article are included in the article's Creative Commons licence, unless indicated otherwise in a credit line to the material. If material is not included in the article's Creative Commons licence and your intended use is not permitted by statutory regulation or exceeds the permitted use, you will need to obtain permission directly from the copyright holder. To view a copy of this licence, visit <http://creativecommons.org/licenses/by/4.0/>.

© The Author(s) 2022